ROYAL SOCIETY
OF CHEMISTRY

PAPER

Check for updates

Synthesis of sulfur-doped carbon quantum dots from Solanum nigrum for ciprofloxacin detection in yogurt samples and antibacterial activity

Shuchen Pei, [ID] [a] Yifan Wang,[a] Shaoyu Cai,[a] Kangli Yan,[a] Kang Luo [ID] *[b] and Yunqi Ma*[c]

In this study, S-CQDs were fabricated through a green and secure hydrothermal process, the carbon source was derived from the traditional Chinese medicinal herb Solanum nigrum and thiourea served as the sulfur precursor. The characterization results indicated that the S-CQDs presented a spherical shape, featuring a mean particle diameter of 3.96 nm and a lattice spacing measuring 0.19 nm. Surface functional groups such as amides, amino groups, and carboxyl groups were identified, contributing to their physicochemical properties. The S-CQDs demonstrated high selectivity and sensitivity toward CIP, spanning a linear detection range covering 0–0.4 μmol L^{-1}. Additionally, these materials displayed substantial antibacterial efficacy against both S. aureus and E. coli, with MIC values of 1.6 mg mL^{-1} and 0.8 mg mL^{-1} for each bacterium, respectively. Mechanistic investigations indicated that the positively charged S-CQDs electrostatically interacted with negatively charged bacterial membranes, disrupting membrane integrity and ultimately leading to bacterial cell death. This work establishes a novel approach for developing multifunctional S-CQDs, highlighting their promising applications in clinical diagnostics, environmental monitoring and antimicrobial therapies.

Introduction

Carbon quantum dots (CQDs), which belong to a group of carbon nanomaterials with dimensions smaller than 10 nm, were first identified in 2004 during the preparation of electrophoretically purified single-walled carbon nanotubes.[1] With the deepening of research in recent years, it has been revealed that CQDs not only allow for straightforward synthesis from organic materials but also boast exceptional water solubility,[2,3] antibacterial activity,[4–7] selectivity[8,9] and sensitivity[10–12] that render them highly versatile across a spectrum of applications, spanning from bioimaging and biosensing to cancer therapy,[13–16] drug delivery,[17] metal ion detection,[18–20] and water treatment.[20,22] Moreover, such is the robustness and tunability of CQDs' fluorescence properties that they are well-suited for fabricating optoelectronic devices, sensors, photocatalytic solar cells, and even smart packaging films.[23–26]

Recent studies have reported a substantial number of CQDs exhibiting antibacterial activity. Research has demonstrated that modified CQDs not only partially inhibit Porphyromonas

gingivalis[27] but also enable the preparation of doped CQDs that exhibit excellent inhibitory effects against Escherichia coli (E. coli) and Staphylococcus aureus (S. aureus).[5] Remarkably, even bacterially derived CQDs show outstanding antibacterial activity against Salmonella typhi, Pseudomonas aeruginosa, and Bacillus subtilis under neutral pH conditions.[28] Collectively, these findings highlight that targeted doping modifications of CQDs may effectively inhibit and inactivate diverse bacterial species.

Central to the antimicrobial mechanisms of antibacterial CQDs is the generation of reactive oxygen species (ROS).[29] Generated through either photoexcitation or inherent redox properties of CQDs, ROS including superoxide, hydrogen peroxide, hydroxyl radicals, and singlet oxygen-exert photodynamic inactivation effects on biomolecules such as lipids, proteins, and DNA. Excessive ROS accumulation not only induces intracellular lipid peroxidation and DNA damage but also disrupts membrane integrity through lipid peroxidation, ultimately triggering cytoplasmic leakage that inhibits bacterial growth and causes cell death;[30] this cascade thereby reduces the development of bacterial resistance. Fundamental to our subsequent antibacterial experiments with S-CQDs lies this pivotal mechanism, which provides critical theoretical support for their design.[31]

Currently, researchers have extensively explored the modification effects of different dopants such as nitrogen, phosphorus, sulfur, and metal elements on CQDs. Among them,

[a]School of Chemistry and Chemical Engineering, Chongqing University of Science and Technology, Chongqing 401331, China

[b]People's Hospital Affiliated to Chongqing Three Gorges Medical College, Chongqing 404037, China. E-mail: kang_luo@live.cn

[c]Department of Pharmacy, Shapingba Hospital, Chongqing University, Chongqing 400032, China. E-mail: mayunqi2012@163.com

nitrogen doping is one of the most in-depth modification methods studied, exhibiting high selectivity in the field of metal ion detection.[21,32] Phosphorus doping optimizes the electrochemical activity of CQDs by regulating their surface charge distribution and electron conduction efficiency, and has become a potential antimicrobial therapy tool due to its photocatalytic function comparable to that of traditional nanoscale semiconductors.[33] Metal element doping is more widely applied in environmental governance, playing a role in antibacterial and pollutant degradation processes; for example, copper-doped carbon quantum dots (Cu-CQDs) can effectively alleviate microbiologically influenced corrosion.[34] In contrast, sulfur-doped CQDs exhibit particularly prominent unique advantages, such as –SH and –C–S–C– can be formed on their surface, which can enhance hydrogen bonding or chelation with target substances, enabling the formation of cross-linked structures with ciprofloxacin, thereby significantly improving the specific fluorescence detection capability for ciprofloxacin.[35] Meanwhile, sulfur-doped CQDs also possess excellent stability and show outstanding detection sensitivity and selectivity towards certain specific compounds.[36,37]

In this study, S-CQDs were fabricated through a green and secure hydrothermal process, the carbon source was derived from the traditional Chinese medicinal herb *Solanum nigrum*, and thiourea served as the sulfur precursor. The S-CQDs demonstrated high selectivity and sensitivity toward CIP. Additionally, these materials displayed substantial antibacterial efficacy against both *S. aureus* and *E. coli*, respectively. This work establishes a novel approach for developing multifunctional S-CQDs, highlighting their promising applications in clinical diagnostics, environmental monitoring and antimicrobial therapies.

Experimental

Materials

Solanum nigrum was purchased from a local supermarket in Chongqing, China. Horseradish peroxidase (HRP) originated from Sinopharm Chemical Reagent Co., Ltd. Phosphate-buffered saline (PBS), hydroxypropyl acrylate (HPA), and 3-(4,5-dimethyl-2-thiazolyl)-2,5-diphenyl-2*H*-tetrazolium bromide (MTT) were all sourced from Merck KGaA. The bacterial strains *E. coli* JM109 and *S. aureus* ATCC6538 were procured from our laboratory collection. BV2 microglioma cells was purchased from Qingqi (Shanghai) Biotechnology Development Co., Ltd. Deionized water was used for preparing all solutions, and all employed chemicals were analytical-grade, conforming to standard specifications.

Characterization methods

Using a JEOL JEM-2100F microscope (Tokyo, Japan), transmission electron microscopy (TEM) and HRTEM (high-resolution TEM) analyses were performed to characterize the samples. XRD. A Nicolet iS5 spectrometer (Thermo Fisher Scientific, Waltham, MA, USA) was used to record FT-IR spectra, whereas the surface makeup of S-CQDs was characterized by X-

ray photoelectron spectroscopy (XPS; ESCALAB Xi+). A Shimadzu RF-5301 PC spectrofluorometer (Kyoto, Japan) was used to acquire fluorescence (FL) spectra, and a Shimadzu UV-1800 spectrophotometer (Japan) was employed for measuring UV-Vis absorption spectra. A microplate reader (Awareness Technology, Florida, USA) was used to conduct MIC assays at 600 nm, while a NanoBrook 90Plus Zeta analyzer (Brookhaven Instruments, USA) measured the zeta potential.

Synthesis of S-CQDs

S-CQDs were synthesized *via* a one-step hydrothermal method. Specifically, 3.0 grams of *Solanum nigrum* and 2.25 grams of thiourea were combined and homogenized in 45 mL of deionized water. The prepared mixture was transferred to a 100 mL Teflon-lined stainless-steel autoclave, sealed, and subjected to hydrothermal treatment at 180 °C for 12 hours. After filtering the resultant suspension through a 0.22 μm filter to remove unreacted solids, the mixture was centrifuged at 8000 rpm for 10 minutes. The obtained supernatant was then dialyzed using a 500 Da dialysis membrane for 12 hours to exclude low-molecular-weight contaminants. After dialysis, the purified S-CQD solution underwent freeze-drying to yield a solid powder, which was stored in a sealed glass vial at 4 °C for subsequent characterization and applications.

Sensitivity and selective detection of ciprofloxacin

The selectivity assessment of S-CQDs was performed by mixing a defined volume of S-CQDs solution with the solutions of different ions, antibiotics, and amino acids, the mixture was then incubated at room temperature for 1 hour. Fluorescence emission spectra were acquired upon excitation at 310 nm. Furthermore, the fluorescence enhancement behavior of S-CQDs was investigated in PBS buffer with increasing ciprofloxacin concentrations. All measurements were conducted in triplicate to ensure methodological reproducibility.

Quantum yield (QY) calculation

Quinine sulfate in 0.1 M H_2SO_4 (QY% = 54, η = 1.33) selected as a standard to calculate the QY of N-CQDs.[29]

$$\varphi_{sample} = \varphi_{st} \times \left(\frac{A_x}{A_y}\right) \times \left(\frac{K_x}{K_y}\right) \times \left(\frac{\eta_x}{\eta_y}\right)^2$$

where φ_{st} is the known quantum yield of quinine sulfate, K_x and K_y are the integrated areas of the emission of N-CQDs and quinine sulfate, A_x and A_y are the UV-absorbance of the sample and the reference, and η is the refractive index of solvent (water: 1.33). The fluorescence quantum yield was 13.2%.

Antibacterial test

Culture of bacterial. Prior to the experiment, *E. coli* and *S. aureus* were cultured in Luria-Bertani (LB) broth medium at 37 °C with shaking at 180 rpm until their OD_{600} at 0.6–0.8, corresponding to the mid-exponential growth phase. The cell density was standardized to 1.5×10^7 CFU mL^{-1} by OD_{600} calibration.

The activated cultures were subsequently stored at 4 °C until for later use.

Assay of antibacterial activity. To evaluate the MIC of S-CQDs, 100 μL of *E. coli* and *S. aureus* bacterial suspensions were individually combined with 100 μL of serially diluted S-CQDs in 96-well plates. Following 12 hours incubation at 37 °C, bacterial growth was assessed by measuring OD_{600}. Following this, 10 μL of MTT solution was introduced into each well, and the plates were further incubated for 20 minutes to assess metabolic activity.

For growth inhibition studies, Bacterial suspensions of *E. coli* and *S. aureus* (1.5×10^7 CFU mL^{-1}) were mixed with serial dilutions of S-CQDs in 10 mL centrifuge tubes, then incubated at 37 °C with continuous shaking at 180 rpm. Growth kinetics were monitored over 24 hours by periodically transferring 200 μL aliquots to 96-well plates at 2 hours intervals, followed by OD_{600} measurement using a microplate reader.

Antibacterial mechanism of S-CQDs. The surface charge characteristics of S-CQDs were analyzed using zeta potential measurements. Both diluted S-CQDs solutions and activated bacterial suspensions were examined to assess their electrostatic properties. Furthermore, the capacity of S-CQDs to produce hydrogen peroxide was quantitatively evaluated through fluorescence spectrophotometric analysis.

***In vitro* cytotoxicity test.** The cytotoxicity of S-CQDs was evaluated using the standard methyl thiazolyl tetrazolium (MTT) assay. First, BV2 microglioma cells were cultured in Dulbecco's Modified Eagle's Medium (DMEM) containing 10% fetal bovine serum. Subsequently, 100 μL of BV2 microglioma cells were taken and seeded into a 96-well plate at a density of 1 × 104 cells per well, followed by incubation in a constant-temperature incubator at 37 °C for 24 hours. Afterwards, S-CQDs with concentrations ranging from 0 to 500 μg mL^{-1} were added to each well, and incubation was continued for another 24 hours. Finally, the cell culture medium was removed, 20 μL of MTT solution (5 mg mL^{-1}) was added to each well, and after 4 hours of incubation, 150 μL of dimethyl sulfoxide (DMSO) was added to dissolve the MTT. The absorbance of the samples was measured using a microplate reader.

Results and discussion

Characterization

The morphology and composition of S-CQDs were characterized using TEM, XRD, FT-IR, and XPS. As depicted in Fig. 1a–d, The S-CQDs display well-dispersed spherical nanostructures with a narrow size distribution (1.51–5.47 nm) and an average diameter of 3.96 nm. HR-TEM analysis clearly demonstrates the presence of well-defined graphitic crystallinity, exhibiting characteristic lattice fringes with a measured *d*-spacing of 0.19 nm. The XRD pattern of S-CQDs shows a broad peak centered at $2\theta \approx 25°$, which can be attributed to the (002) plane of graphene. The obtained results are consistent with the corresponding TEM results mentioned above.

FT-IR was utilized to characterize the surface functional moieties present on the S-CQDs. In Fig. 2a, originating from the O–C–O stretching vibration is the absorption peak at 604 cm^{-1},
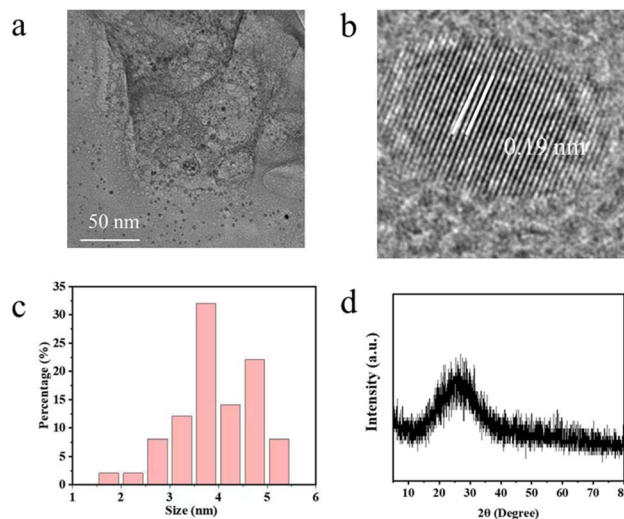

Fig. 1 (a) TEM image of S-CQDs; (b) HRTEM image of S-CQDs; (c) the diameter distribution of S-CQDs; (d) XRD image of S-CQDs.

whereas the peak at 1043 cm^{-1} is due to superimposed contributions from C–O–C, C–O and –SO$_3^-$ groups. Corresponding to C–N bonds, the absorption band at 1080 cm^{-1} provides evidence for the presence of nitrogen-containing functional groups on the CQD surface. Attributed to the symmetric stretching vibration of COO$^-$ groups, the 1402 cm^{-1} peak contrasts with the 1635 cm^{-1} absorption, which probably stems from C–H stretching or bending motions. Additionally, the broad peak centred at 3375 cm^{-1} is ascribed to N–H stretching or bending modes, further corroborating the nitrogen-rich surface chemistry of the S-CQDs.

XPS was conducted to quantitatively determine the elemental constituents and their relative atomic distribution in the S-CQDs. As depicted in Fig. 2b, XPS wide-scan analysis of S-CQDs reveals four characteristic peaks at binding energies corresponding to S (4.11 at%), C (58.47 at%), N (7.03 at%), and
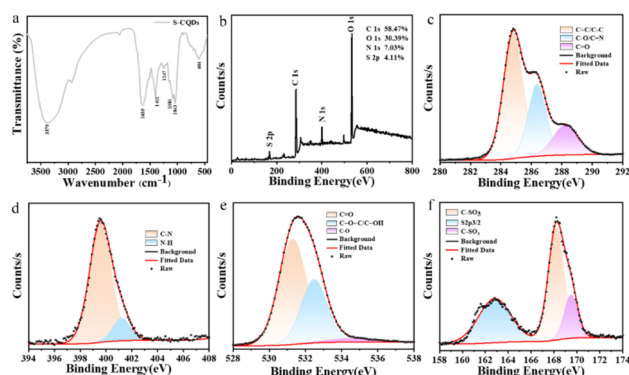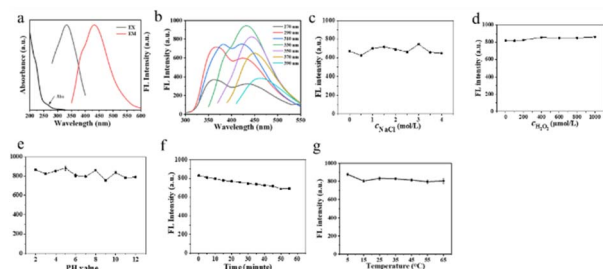

Fig. 2 (a) FTIR spectrum of S-CQDs revealing surface functional groups; (b) XPS survey spectrum of S-CQDs; (c) high-resolution XPS spectra of C1s core level in S-CQDs; (d) high-resolution XPS spectra of N1s core level in S-CQDs; (e) high-resolution XPS spectra of O1s core level in S-CQDs; (f) high-resolution XPS spectra of S2p core level in S-CQDs.

Fig. 3   (a) Excitation, emission, and UV-Vis absorption characteristics of S-CQDs (b) emission spectra of S-CQDs under different excitation wavelengths. (c) FL response of S-CQDs to NaCl solution with different concentrations. (d) FL response of S-CQDs to varying concentrations of H_2O_2. (e) FL response of S-CQDs to different pH and (f) FL response of S-CQDs to continuous illumination. (g) FL response of S-CQDs to different temperature.

Fig. 4   The FL intensity of S-CQDs with different interfering substance: (a) ions; (b) amino acids and antibiotics; (c) the change trend of the FL intensity at different CIP concentrations; (d) blank control experiments for S-CQDs; (e) the FL intensity of S-CQDs at different CIP concentrations (0.01–0.1 μmol L^{-1}), the inset illustrated the linear relationship between $(F_0 - F)/F_0$ and the concentration of CIP.
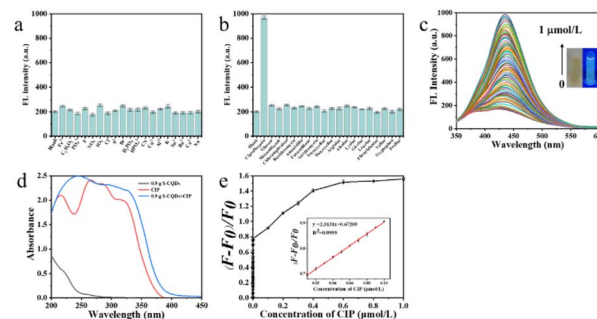
O (30.39 at%), confirming the successful incorporation of heteroatoms. High-resolution C1s XPS analysis reveals three deconvoluted peaks at binding energies of 284.2 eV (C=C/C–C), 286.4 eV (C–O/C–N), and 288.4 eV (C=O), as shown in Fig. 2c. The high-resolution N1s spectrum in Fig. 2d resolves into two distinct components at 399.3 eV (C–N) and 401.1 eV (N–H), unambiguously demonstrating the coexistence of amine and amide functional groups. The O1s spectrum, illustrated in Fig. 2e, comprises three contributions: 530.9 eV (C=O), 532.2 eV (C–O–C/C–OH), and 534.8 eV (C–O). The high-resolution S2p spectrum (Fig. 2f) resolves into three characteristic doublets: the primary component at 162.9 eV ($S2p_{3/2}$) represents reduced sulfur species, while the peaks at 168.1 eV (C–SO_3^-) and 169.5 eV (C–SO_4) confirm the presence of oxidized sulfur moieties. These analytical results collectively demonstrate the co-existence of both nitrogenous (amine/amide) and oxygenated (hydroxyl/carbonyl/sulfonic) functional groups on S-CQD surfaces, which fundamentally govern their unique physicochemical properties and biological activities.

The optical stability of S-CQDs

The optical characteristics of S-CQDs were systematically examined through photoluminescence spectroscopy and UV-Vis absorption measurements. As exhibited in Fig. 3a, the optimum excitation and emission wavelengths for S-CQDs are 335 and 425 nm, respectively. The intensity of the emission peaks varies depending on the relevant excitation wavelength, which in Fig. 3b can be in the range of 270–390 nm. In Fig. 3c–f, the fluorescence intensity was almost unchanged under different concentrations of NaCl and H_2O_2 aqueous solutions, different pH, stable light (330 nm) and temperature. These results quantitatively confirm the excellent stability of the S-CQDs.

Detection effect of S-CQDs on ciprofloxacin

The photostability of S-CQDs was rigorously examined under different chemical conditions, encompassing metal ions, as well as various antibiotics and amino acids. As depicted in Fig. 4a and b, The S-CQDs demonstrated remarkable selectivity,

exhibiting substantial fluorescence enhancement exclusively upon ciprofloxacin (CIP) addition, while remaining unaffected by other tested ions and biochemical species. To quantify the fluorescence intensity changes induced by CIP, the interaction kinetics were investigated by monitoring fluorescence changes after sequential addition of CIP (0–1000 μM final concentration) to S-CQDs solutions, with spectra acquired after 5 min equilibration at each concentration. As illustrated in Fig. 4c, the fluorescence intensity of S-CQDs progressively increased with higher CIP concentrations. To further validate the detection stability, a blank control (without CIP) was measured, revealing a substantial reduction in fluorescence intensity (Fig. 4d). In Fig. 4e, the standard curve for S-CQDs response to CIP demonstrates a good linear relationship between the fluorescence intensity ratio $(F - F_0)/F_0$ and CIP concentration in the range of 0.01–0.1 μmol L^{-1}. The linear regression equation was determined to be: $(F - F_0)/F_0 = 2.3131x + 0.67209$, $R^2 = 0.9995$ (F and F_0 denote the presence and absence of CIP, respectively).

Detection in real samples

For real-sample applications, we spiked yogurt samples with different concentrations of CIP standard solutions for detection in Table 1. The S-CQDs sensor demonstrated excellent recovery rates ranging from 98.00% to 100.63% in these analyses. This shows that S-CQDs serve as an economical and environmentally friendly carbon nanosensor for reliable quantitative detection of CIP.

Table 1   Recovery rate of CIP in yogurt

Sample	Added (μM)	Test (μM)	Recovery rate (%)	RSD (%)
Yogurt	0.1	0.098	98.00	0.016
	0.2	0.196	98.00	0.008
	0.4	0.395	98.75	0.023
	0.6	0.603	100.50	0.026
	0.8	0.805	100.63	0.030
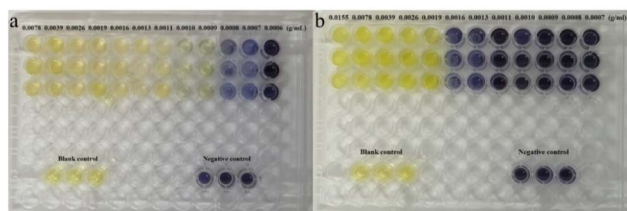
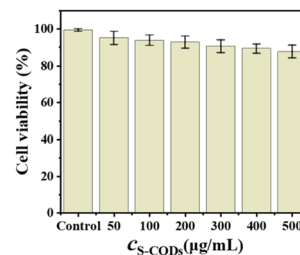Fig. 5 The antibacterial ability of S-CQDs on (a) *E. coli* and (b) *S. aureus*.
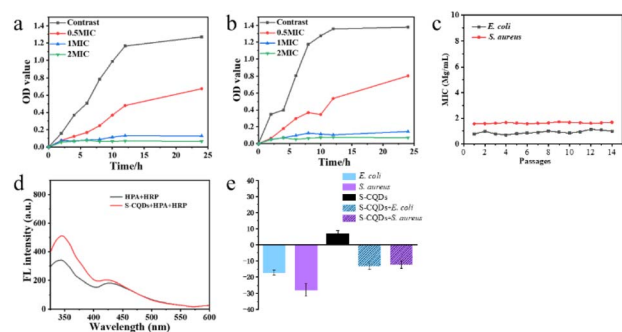

Fig. 6 (a) The inhibition curve against *E. coli*; (b) the inhibition curve against *S. aureus*; (c) the drug resistance of S-CQDs; (d) the generated ROS of S-CQDs hydrogen peroxide; (e) zeta potential distribution of S-CQDs.

Fig. 7 Cell viability under different concentrations of S-CQDs.

The antibacterial efficacy of S-CQDs

The antimicrobial efficacy of S-CQDs toward Gram-negative (*E. coli*) and Gram-positive (*S. aureus*) bacteria was evaluated *via* the microdilution method. The MTT assay was employed to assess the MIC, in which bacterial suspensions of both strains were exposed to various S-CQDs concentrations, subjected to a 12 hours incubation, and then stained with MTT. The MIC values of S-CQDs against *E. coli* and *S. aureus*, as presented in Fig. 5a and b, were 0.8 mg mL^{-1} and 1.6 mg mL^{-1}, respectively, demonstrating a concentration-dependent antibacterial effect.

For time-dependent antibacterial analysis, both bacterial strains' suspensions were exposed to S-CQDs at 0.5× the MIC, 1× the MIC, and 2× the MIC, with OD$_{600}$ values tracked to evaluate bactericidal kinetics. As shown in Fig. 6a–c, treatment with 0.5× MIC S-CQDs induced partial inhibition of growth in both *E. coli* and *S. aureus*. At 1× MIC, a pronounced suppression of bacterial growth was observed for both species. Notably, even at 2× MIC, neither *E. coli* nor *S. aureus* developed drug resistance to S-CQDs, underscoring the potent and sustained antibacterial efficacy of the material across escalating concentrations.

Antibacterial mechanism of S-CQDs

To further explore the antibacterial mechanism of S-CQDs, we assessed their potential to produce ROS. In the presence of horseradish peroxidase (HRP), S-CQDs catalyzed the oxidation of 4-hydroxyphenylacetic acid (HPA), forming a ROS-sensitive fluorescent product (λ_{em} = 450 nm), by which H$_2$O$_2$

production could be quantitatively monitored. As shown in Fig. 6d, under light irradiation, the fluorescence intensity initially decreased but gradually increased after 20 minutes, confirming the light-triggered generation of H$_2$O$_2$ by S-CQDs. Zeta potential measurements (Fig. 6e) revealed that *Staphylococcus aureus* and *Escherichia coli* exhibited surface charges of −28.19 mV and −17.83 mV, respectively, while S-CQDs carried a positive charge. After treatment with S-CQDs, the surface charges of both bacterial strains shifted toward less negative values, suggesting that the positively charged S-CQDs disrupted bacterial membrane permeability and integrity, thereby facilitating intracellular ROS accumulation. These results collectively demonstrate that S-CQDs penetrate bacterial membranes and induce oxidative stress through ROS generation, leading to structural damage and eventual cell death.

In vitro cytotoxicity test

To simulate and predict the biological responses of S-CQDs, we evaluated their cytotoxicity using the MTT assay. As shown in Fig. 7, within the tested concentration range of 50–500 μg mL^{-1}, S-CQDs had no or negligible effect on the growth of BV2 microglioma cells. The results obtained indicate that S-CQDs are biocompatible, with the survival rate of treated cells exceeding 80%.

Conclusions

In this study, S-CQDs were fabricated through a green and secure hydrothermal process, the carbon source was derived from the traditional Chinese medicinal herb *Solanum nigrum*, and thiourea served as the sulfur precursor. Morphological analysis showed that the S-CQDs possessed a spherical shape, featuring an average particle diameter of 3.96 nm and a lattice spacing of 0.19 nm. Surface functional groups such as amides, amino groups, and carboxyl groups were identified, contributing to their physicochemical properties. The S-CQDs demonstrated high selectivity and sensitivity toward CIP, with their linear detection range covering 0–0.4 μmol L^{-1}. Significant antibacterial activity of the S-CQDs toward *E. coli* and *S. aureus* was evidenced by MIC determinations, with the minimum inhibitory concentration for *E. coli* recorded as 0.8 mg mL^{-1} and that for *S. aureus* as 1.6 mg mL^{-1}. Mechanistic investigations indicated that the positively charged S-CQDs electrostatically interacted with negatively charged bacterial membranes, disrupting membrane integrity and ultimately leading to bacterial

cell death. This work establishes a novel approach for developing multifunctional S-CQDs, highlighting their promising applications in clinical diagnostics, environmental monitoring and antimicrobial therapies.

Author contributions

All authors contributed to the study conception and design. Shuchen Pei: Validation, writing-review & editing. Yifan Wang: Formal analysis and writing-original draft. Shaoyu Cai: Data curation. Kangli Yan: Software. Kang Luo: Methodology and project administration. Yunqi Ma: Writing-review & editing.

Conflicts of interest

There are no conflicts to declare.

Data availability

All relevant data are within the paper.

Acknowledgements

Notes and references

1 X. Xu, R. Ray, Y. Gu, H. J. Ploehn, L. Gearheart, K. Raker and W. A. Scrivens, *J. Am. Chem. Soc.*, 2004, **126**(40), 12736–12737.
2 Y. Guo, R. Wang, C. Wei, Y. Li, T. Fang and T. Tao, *Food Chem.*, 2023, **415**, 135749.
3 J. Kong, Y. Wei, F. Zhou, L. Shi, S. Zhao, M. Wan and X. Zhang, *Molecules*, 2024, **29**(9), 2002.
4 M. Alavi, E. Jabari and E. Jabbari, *Expert Rev. Anti-Infect. Ther.*, 2021, **19**(1), 35–44.
5 S. Chai, L. Zhou, S. Pei, Z. Zhu and B. Chen, *Micromachines*, 2021, **12**(9), 1116.
6 Y. Wu, C. Li, H. C. van der Mei, H. J. Busscher and Y. Ren, *Antibiotics*, 2021, **10**(6), 623.
7 C. Zhao, X. Wang, L. Yu, L. Wu, X. Hao, Q. Liu, L. Lin, Z. Huang, Z. Ruan, S. Weng, A. Liu and X. Lin, *Acta Biomater.*, 2022, **138**, 528–544.
8 S. Zhao, X. Lai, F. Liu and L. Chen, *Ecotoxicol. Environ. Saf.*, 2022, **244**, 114069.
9 P. Singh, S. Arpita Kumar, P. Kumar, N. Kataria, V. Bhankar, K. Kumar, R. Kumar, C. T. Hsie and K. S. Khoo, *Nanoscale*, 2023, **15**(40), 16241–16267.
10 S. W. Park, T. E. Kim and Y. K. Jung, *Anal. Chim. Acta*, 2021, **1165**, 338513.
11 X. Feng, G. Han, J. Cai and X. Wang, *J. Colloid Interface Sci.*, 2022, **607**, 1313–1322.

12 J. Zhang, J. Deng, J. Zheng, Y. Ma, H. Luo, X. Luo, C. Hou and D. Huo, *Food Chem.*, 2023, **422**, 136080.
13 M. O. Caglayan, F. Mindivan and S. Șahin, *Crit. Rev. Anal. Chem.*, 2022, **52**(4), 814–847.
14 A. Vibhute, O. Nille, G. Kolekar, S. Rohiwal, S. Patil, S. Lee and A. P. Tiwari, *J. Fluoresc.*, 2022, **32**(5), 1789–1800.
15 S. Das, S. Mondal and D. Ghosh, *Front. Bioeng. Biotechnol.*, 2023, **11**, 1333752.
16 P. Zhu, X. Zhao, Q. Zhu, X. Han, Y. Tang, S. Liao, Z. Guo and Z. Wang, *Chem. Eng. J.*, 2023, **470**, 144042.
17 M. Bartkowski, Y. Zhou, M. Nabil Amin Mustafa, A. J. Eustace and S. Giordani, *Chemistry*, 2024, **30**(19), e202303982.
18 M. Batool, H. M. Junaid, S. Tabassum, F. Kanwal, K. Abid, Z. Fatima and A. T. Shah, *Crit. Rev. Anal. Chem.*, 2022, **52**(4), 756–767.
19 Y. Tang, Q. Xu, X. Zhang, R. Zhu and N. Zhao, *Nano Res.*, 2024, **17**(11), 10109–10118.
20 I. A. Revesz, S. M. Hickey and M. J. Sweetman, *J. Mater. Chem. B*, 2022, **10**(23), 4346–4362.
21 U. A. Rani, L. Y. Ng, C. Y. Ng and E. Mahmoudi, *Adv. Colloid Interface Sci.*, 2020, **278**, 102124.
22 M. Nasrollahzadeh, M. Sajjadi, S. Iravani and R. S. Varma, *Chemosphere*, 2021, **263**, 128005.
23 M. J. Molaei, *Talanta*, 2019, **196**, 456–478.
24 D. Örenli, S. C. Kaçar, F. Öztürk, P. E. Erden and E. Kılıç, *Anal. Biochem.*, 2023, **662**, 115002.
25 W. Zhang, B. Wu, Z. Li, Y. Wang, J. Zhou and Y. Li, *Spectrochim. Acta, Part A*, 2020, **229**, 117931.
26 B. D. Mansuriya and Z. Altintas, *Sensors*, 2020, **20**(4), 1072.
27 J. Wang, Y. Wang, H. Zhang, W. Zhu and L. Liu, *Exp. Biol. Med.*, 2023, **248**(23), 2227–2236.
28 M. Pant, S. Kumar, K. Kiran, N. S. Bisht, V. Pande and A. Dandapat, *RSC Adv.*, 2023, **13**(14), 9186–9194.
29 L. Lai, X. Huang, W. Sun, X. Chen, S. Pei, S. Chai and J. Chen, *Russ. J. Gen. Chem.*, 2022, **92**(10), 2178–2185.
30 C. Huang, M. Duan, Y. Shi, H. Liu, P. Zhang, Y. Zuo, L. Yan, Y. Xu and Y. Niu, *J. Colloid Interface Sci.*, 2023, **645**, 933–942.
31 C. Chu, C. Zou, Y. Qiu, D. Hou, Y. Deng and X. Wang, *Dalton Trans.*, 2023, **52**(23), 7982–7991.
32 Y. Venkatesh, P. Naidu and P. Rao, *Res. Chem. Intermed.*, 2025, **51**, 2621–2643.
33 S. Hindi, J. Sabir, U. Dawoud, I. Insmail, K. Asily and Z. Mirdad, *Polymers*, 2023, **15**(12), 2660.
34 S. T. Kalajahi, B. Rasekh, F. Yazdian, J. Neshati and L. Taghavi, *Environ. Sci. Pollut. Res. Int.*, 2020, **27**(32), 40537–40551.
35 Z. Li, Z. Zhou, J. Wang, T. Tao and Y. Fu, *Nanotechnology*, 2023, **34**(39), 395503.
36 F. Du, Z. Cheng, W. Tan, L. Sun and G. Ruan, *Spectrochim. Acta, Part A*, 2020, **226**, 117602.
37 M. Kaur, M. Bhattacharya and B. Maity, *RSC Adv.*, 2025, **15**(25), 19884–19898.